ARTICLES
PUBLISHED ONLINE: 19 APRIL 2009 | DOI: 10.1038/NMAT2430
nature materials

Spraying asymmetry into functional membranes layer-by-layer

Kevin C. Krogman[1,2], Joseph L. Lowery[1,2], Nicole S. Zacharia[2,3], Gregory C. Rutledge[1,2] and Paula T. Hammond[1,2]*

As engineers strive to mimic the form and function of naturally occurring materials with synthetic alternatives, the challenges and costs of processing often limit creative innovation. Here we describe a powerful yet economical technique for developing multiple coatings of different morphologies and functions within a single textile membrane, enabling scientists to engineer the properties of a material from the nanoscopic level in commercially viable quantities. By simply varying the flow rate of charged species passing through an electrospun material during spray-assisted layer-by-layer deposition, individual fibres within the matrix can be conformally functionalized for ultrahigh-surface-area catalysis, or bridged to form a networked sublayer with complimentary properties. Exemplified here by the creation of selectively reactive gas purification membranes, the myriad applications of this technology also include self-cleaning fabrics, water purification and protein functionalization of scaffolds for tissue engineering.

Naturally occurring membranes, such as those found in plants, cell walls and organs including the epidermis and intestinal wall, derive their ability to segregate two different environments largely from the asymmetry established by their protein constituents[1,2]. Instead of functioning as a uniform barrier, the cross-section of these membranes varies according to their purpose, enabling interior and exterior portions of the membrane to serve very different roles. Segregation of structure is also observed in porous polymer membranes, where a thin effective separation layer is formed at the upstream surface of the membrane, while the bulk material remains porous and less densely packed[3]. Although identical in chemical composition, asymmetric arrangement of two morphologies provides the membrane with mechanical robustness whereas separation is regulated predominantly by the thin barrier layer of material near the surface. Aside from mechanical integrity, however, the phase inversion technique used to generate asymmetric polymer membranes does not introduce functional activity to the bulk matrix, thereby underutilizing the full potential of the substrate material. Here we present a novel process capable of two distinct flow-rate-dependent modes of electrostatic deposition by which multiple functionalities can be introduced into a single engineered textile. Similar to the way in which many naturally occurring membranes simultaneously regulate mass transfer and undergo chemical reactions with solute molecules, this technique enables portions of the textile to act as an inert barrier while the bulk material acts as a high-surface-area scaffold capable of a wide variety of functionalities.

The layer-by-layer (LbL) assembly technique enables the deposition of ultrathin uniform films by the sequential electrostatic deposition of charged polymers[4–6], nanoparticles[7–10], biological templates[11] or biologically active species[12]. An inherently charged substrate is serially exposed to solutions of oppositely charged species, which adsorb to the developing film at rates that enable nanometre-scale control of the film thickness[13]. In recent years, an extension of this technique has been developed by which solutions of charged species are sprayed onto the desired substrate[14–16]. Similar to the traditional dipping process, assembly occurs through electrostatic interactions between areas of local charge density on oppositely charged species, but process times can be reduced more than 25-fold by convectively transporting charged species to the surface. Planar non-porous substrates such as silicon and glass are readily coated by either technique and, when exposed to similar solutions, show ostensibly similar growth rates and final film properties[14,16]. Electrospun (ES) fibres enable the generation of porous polymer scaffolds, which can be tuned for fibre size and surface area[17] and chemically modified using a number of methods[18–20]. By drawing a pressure gradient across porous substrates during the spray-assisted layer-by-layer (spray-LbL) process, we have found that highly conformal coatings can be developed on individual fibres, wires or pores throughout the thickness of the bulk porous substrate. This process retains the flexibility, speed and ambient processing conditions that make spray-LbL an attractive deposition technique, and is capable of creating exceptionally high-surface-area coatings; applications of relevance include self-cleaning photocatalysis[19,21,22], conformal surface passivation[23–26] for corrosion protection, or biocatalytic membranes for pharmaceutical or biofuel applications.

To demonstrate the conformal coating of individual fibres within a material, parallel-plate electrospinning was used to create flexible non-woven mats of microscale nylon 6,6 fibres (average fibre diameter $D = 1.64 \pm 0.25\,\mu\text{m}$) from hexafluoroisopropanol solutions (Fig. 1a,b)[27]. Selecting poly(dimethyldiallylammonium chloride) (PDAC) as the cationic species and amphoteric titanium dioxide nanoparticles (which have been synthesized at a pH above the isoelectric point) as the anionic species, a sprayed deposition can be performed. Chosen for its photocatalytic capabilities, this system presents an ideal candidate for catalysis applications by implementing a surface coating on a high-surface-area scaffold.

---

[1]Department of Chemical Engineering, Massachusetts Institute of Technology, Cambridge, Massachusetts 02139, USA, [2]Institute for Soldier Nanotechnologies, Massachusetts Institute of Technology, Cambridge, Massachusetts 02139, USA, [3]Department of Materials Science and Engineering, Massachusetts Institute of Technology, Cambridge, Massachusetts 02139, USA. *e-mail: hammond@mit.edu.

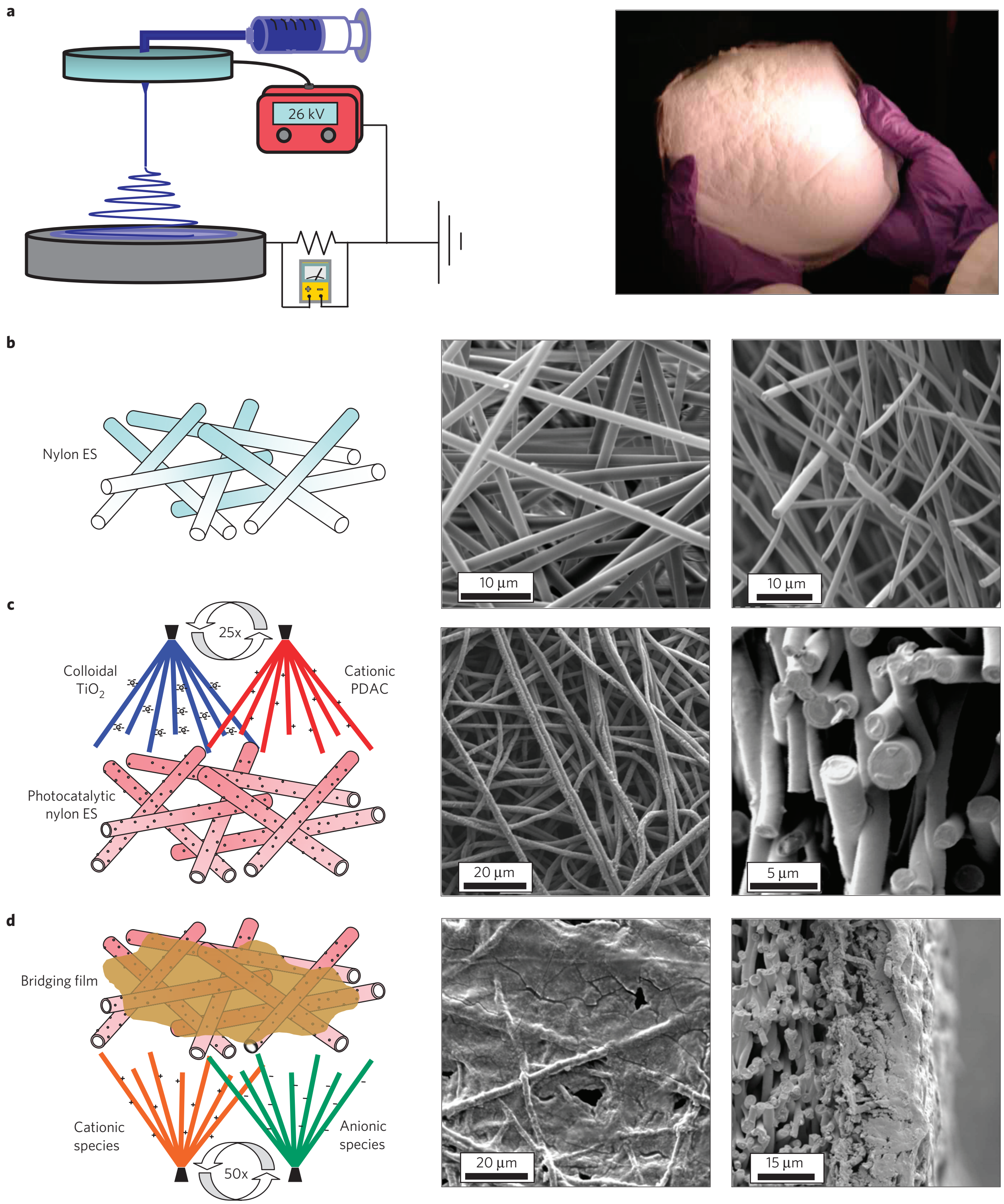

Figure 1 | Demonstration of multifunctionalization process on ES mats. a, The parallel-plate electrospinning technique (diagram, left) is used to create nylon 6,6 ES mats of 8–10 inch diameter (right). **b**, Schematic representation and top-down (centre column) and cross-sectional (far right) scanning electron micrographs. **c**, The technique of spraying in concert with a pressure gradient across the mat is demonstrated to create $(PDAC/TiO_2)_{25}$ conformal coatings on individual fibres. Conformal coatings are of uniform cross-section independent of spray direction, and smoothly coat the length of the fibres. **d**, Spraying in the absence of a pressure gradient to deposit $(PDAC/SPS)_{50}$ coating bridges pores on the mat surface. Heavy bridging occurs after relatively few deposition cycles, and this can be carried out using a variety of charged species to affect the functionality of the final membrane.

Imposing a pressure gradient across the ES material during the deposition generates a controllable convective flow rate, which was found to have a profound effect on the geometry of the developing film. Recalling $\mathrm{Re_d} \approx 6$ as the critical diameter-based Reynolds number for flow separation from the downstream side of a cylinder[28], surprising agreement with the correlation is observed. At $\mathrm{Re_d} = 6.5$ film growth is observed only near the stagnation point on the front of the cylindrical fibres (Fig. 2a); however, as

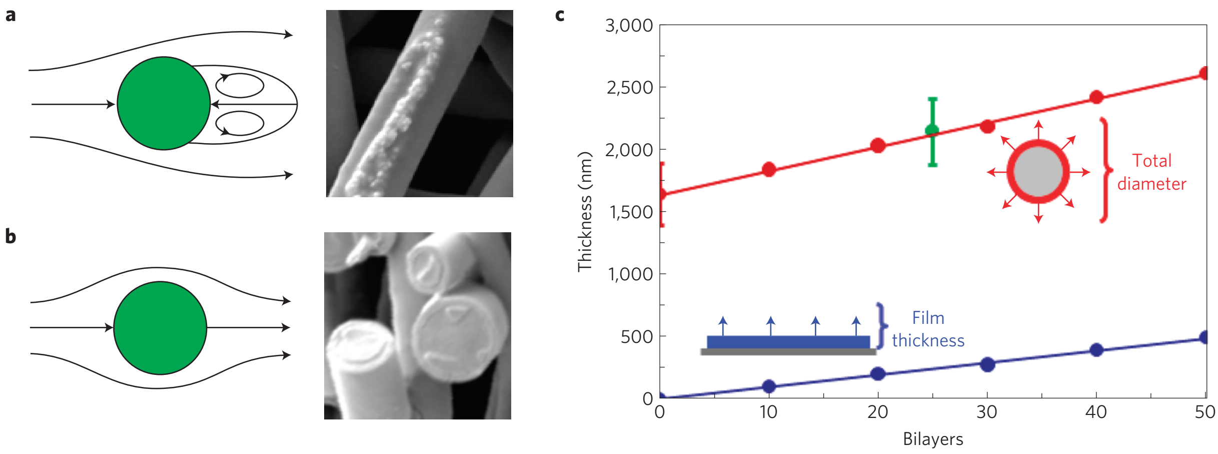

Figure 2 | Growth mechanism as a function of flow rate past ES fibres. a, For packed bed Reynolds numbers $\mathrm{Re_d} = (DV_s)/((1-\varepsilon)\nu) > 6$ (where V_s is the superficial fluid velocity, $\varepsilon = 0.85$ is the void fraction of the ES mat and $\nu = 15.7 \times 10^{-6}\ \mathrm{m^2\ s^{-1}}$ is the kinematic viscosity of air at 300 K), flow separation of the streamlines from the back side of the fibre occurs. At these fluid velocities (scanning electron micrograph taken for $\mathrm{Re_d} \approx 6.5$), LbL deposition is observed to occur only near the leading-edge stagnation point on the fibres. **b**, As the velocity is decreased and $\mathrm{Re_d}$ becomes subcritical, the absence of flow separation enables viscous forces to uniformly deposit polyelectrolyte molecules evenly around the fibre circumference (cross-sectional scanning electron micrograph taken at $\mathrm{Re_d} \approx 1.7$). **c**, The growth profile observed for $(\mathrm{PDAC/TiO_2})_n$ deposited on planar silicon is plotted in blue, and indicates a rate of 9.6 nm per cycle. Assuming that conformal growth is due to a similar mechanism for $\mathrm{Re_d} < 6$, the expected incremental increase in average fibre diameter is plotted in red starting from the observed initial fibre diameter. Average fibre diameter (red line) is expected to grow twice as rapidly as a planar film (blue line) because the deposited layer is counted twice, once from each side of the fibre, by this measurement. Remarkable agreement is observed for the empirical mean and standard deviation of ES fibres treated with $(\mathrm{PDAC/TiO_2})_{25}$, plotted in green. Error bars represent plus or minus one standard deviation in thickness as observed in scanning electron micrographs.

$\mathrm{Re_d}$ becomes subcritical, uniform coatings develop conformally on individual fibres within the mat (Fig. 2b). The coating does not show preference toward the direction of flow (Fig. 1c), but grows linearly (Fig. 2c) at rates similar to those observed on planar substrates (9.6 nm/cycle; ref. 29). This indicates that viscous forces are responsible for species deposition, not line-of-sight impact as observed at higher $\mathrm{Re_d}$ values. Furthermore, on the basis of the spray-LbL technique, conformal coatings can be created rapidly and uniformly even on large substrate areas using this technique. From electron microscopy, it is clear that the nanofibres are each individually coated with a concentric and uniform shell of polymer multilayer, and that the shell is of consistent thickness independent of fibre diameter or position within the ES cross-section (≈0.5 mm thick).

In the absence of a pressure gradient (that is, $\mathrm{Re_d} = 0$), the conformally coated mats can be further processed using the same spray-LbL technique. Instead of convectively penetrating into the ES matrix, polyelectrolyte chains arriving at the material's surface begin to fill the gaps between fibres. As serial deposition continues the coating grows laterally, filling interstitial voids. After only 50 sequential alternations between the cationic species PDAC and a suitably strong polyelectrolyte anionic species such as poly(sodium 4-styrenesulfonate) (SPS), the bridging of surface voids is nearly complete (Fig. 1d). It is perhaps surprising that polyelectrolytes with hydrodynamic sizes on the order of 50 nm are able to occlude 10–20 µm gaps between fibre supports; however, without a convective force driving polyelectrolyte transport throughout the porous network, surface fibres act as an electrostatic net catching the ≈5 µm droplets between nearby fibres through favourable interfacial interactions. Fibre spanning ensues, and bridges efficiently build across the larger pores as the LbL cycle is repeated. As a result, penetration is restricted to 20–30 µm at the surface of the nylon matrix. It should be noted that we believe that the geometry of the ES material plays a crucial role in the bridging process as well. In this demonstration impinging droplets of solution are of a similar order of magnitude in size as the inter-fibre voids, and vary in charge density. At this scale, fluidic properties such as solid–liquid contact may play an equally important role as electrostatics during the bridging process. The upper limitation on bridgeable pore size, if any, will yield further insight into the underlying mechanisms of this type of growth, and will be the subject of future investigation.

The flexibility of this technique is further demonstrated by extending the choice of bridging materials to include polyelectrolyte solutions at pH values drastically different from pH 10, at which $(\mathrm{PDAC/TiO_2})_n$ deposition was conducted. When PDAC/SPS in the previous example is replaced by the polyelectrolyte system of poly(amidoamine) (PAMAM) and poly(acrylic acid) (PAA) titrated to pH 4, the conformal $(\mathrm{PDAC/TiO_2})$ coating remains intact and unaffected. Prolonged exposure to pH 4 solutions in traditional LbL dipping baths would normally lead to loss of ionization of titania nanoparticles (pI = 6), exfoliation and eventual deconstruction and destabilization of $(\mathrm{PDAC/TiO_2})_n$ coatings, severely restricting the range of available pH conditions for processing. The spray-LbL process is significantly more rapid, and the treated mat is never subjected to prolonged soak exposure times at potentially unfavourable pH, lending greater flexibility to the range of coatings that can be applied to the same substrate sample.

To demonstrate the advantages to material design and engineering that this technique presents, we have investigated the application of multifunctionalized ES mats as self-cleaning materials that can provide toxic-chemical protection to the wearer while maintaining comfort and breathability in the form of water-vapour permeability. The goal of this application is to engineer a selectively reactive membrane with tunable mass-transfer properties. Deposited as described above, the conformal application of a photocatalytic film in the presence of a pressure gradient (hereon written $\mathrm{vac(PDAC/TiO_2)_{25}}$) onto the fibres of an ES nylon mat increases the active surface area of smooth as-spun fibres from 2.02 to 48.75 $\mathrm{m^2\ g^{-1}}$ as determined by Brunauer–Emmett–Teller (BET) surface-area analysis. BET-determined values were consistently found to be within 10% of those calculated from scanning

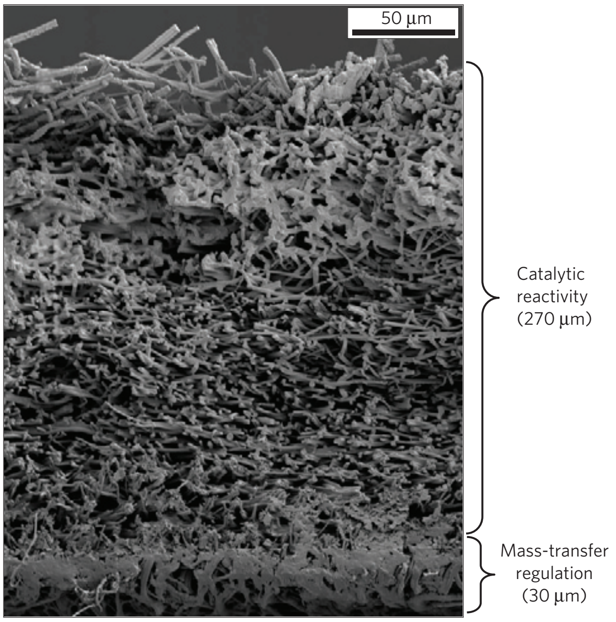

Figure 3 | Entire cross-section of a multifunctionalized ES membrane. An ES nylon sample that has been treated with $(PDAC/TiO_2)_{25}$ in the presence of a pressure gradient to create a high-surface-area photocatalytic region, followed by $(PAMAM/PAA)_{50}$ treatment in the absence of a gradient to create a CEES transport barrier, can be seen in its entirety. Closely resembling an asymmetric polymer membrane for high-efficiency gas separation, only 30 µm, or roughly 10% of the membrane, near the surface is responsible for regulating mass transport, and the remainder of the membrane is free to act as a high-surface-area scaffold for photocatalysis as well as mechanical support for the relatively thin barrier region. Flux can be closely controlled by tuning the content and thickness of the barrier region, producing an optimal residence time for catalytic degradation to occur.

electron microscopy measurements and the geometric relationship (equation (1)) for untreated as-spun samples of both nylon and poly(ε-caprolactone).

$$\frac{A_{\mathrm{surface}}}{\mathrm{mass}}=\frac{2}{R_{\mathrm{fibre}}\rho_{\mathrm{material}}} \tag{1}$$

where R_{fibre} and ρ_{material} refer to the average radius of ES fibres and the density of the bulk mat respectively. The 25-fold increase in surface area is directly due to the conformal coating, the outermost surface layer of which is nanoparticles, as the LbL spray sequence concludes with the anionic species (in this case colloidal TiO_2), now encasing the smooth fibres originally generated during the intense whipping of the electrospinning process. Treated samples were subjected to photocatalytic testing by mounting the mat in between a sealed vapour space containing a saturated vapour of chloroethyl ethyl sulphide (CEES), a simulant for the chemical warfare agent HD mustard gas, and a stream of clean air[29]. By comparing the flux of CEES in the air stream with and without ultraviolet irradiation on the sample, the photocatalytic capability of the treated material can be quantified,

$$\mathrm{capability}=1-\frac{\int_{t_0}^{t_\infty}[\mathrm{permeant}]_{\mathrm{ultraviolet}}\,\mathrm{d}t}{\int_{t_0}^{t_\infty}[\mathrm{permeant}]_{\mathrm{dark}}\,\mathrm{d}t} \tag{2}$$

where the permeant concentrations refer to the concentration of CEES in the air stream below the sample and t_0 and t_∞ define the start and stop times of the permeation test respectively. An ideal sample will have a photocatalytic capability of 1.0, as the net flux of CEES during the ultraviolet-illuminated test approaches zero, whereas a material with no photocatalytic capability will rate 0.0. ES nylon treated with vac$(PDAC/TiO_2)_{25}$ shows high surface area for catalytic reaction, degrading 15% of the CEES dosage when exposed to ultraviolet light, but the reaction remains rate limited by the rate of adsorption of CEES onto the fibre surfaces, enabling significant amounts of CEES contaminant to move diffusively through the highly porous mat. (Note: to confirm that TiO_2 is necessary for CEES degradation a negative control test using untreated nylon under ultraviolet light was conducted. This test also served as a leak control test of the permeation cell. The integrals in the numerator and denominator of the ‘photocatalytic capability’ calculation were within 2% of each other, confirming the reproducibility of the test process as well as the necessity of TiO_2 in the degradation process.) Placing the functionalized ES material in series with a non-porous barrier material such as Saran 8 (a biaxially oriented monolayer film of poly(vinylidene chloride)) eliminates rapid vapour diffusion through the matrix. Acting as diffusive resistance and restricting mass transfer, Saran increases the residence time of CEES molecules in the photocatalytic matrix. Consequently, the observed photocatalytic capability increases to 87%. This scenario illustrates the traditional trade-off of chem-protective materials: chemical barriers suppress toxic chemical penetration, but in the process suppress transport of other small molecules such as water vapour. ES nylon+vac$(PDAC/TiO_2)_{25}$ is highly porous and enables water-vapour flux at a rate of 14.3 kg m^{-2}-d^{-1}, but is able to degrade only 15% of a saturated CEES dosage. Placing it in series with a Saran barrier significantly increases the catalytic residence time, but to achieve the resultant 87% CEES deactivation we decrease the water vapour flux by 99%.

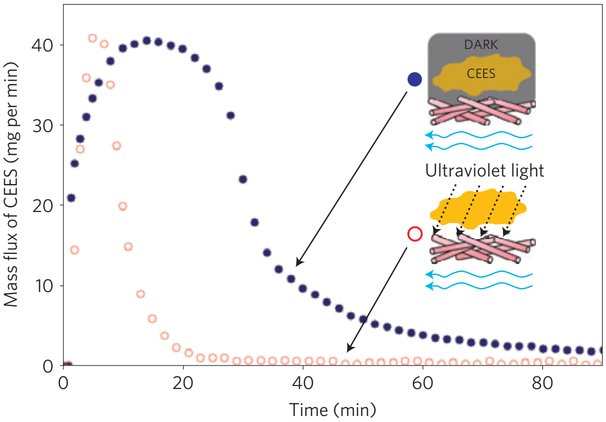

Figure 4 | CEES permeation test results. An ES nylon sample is treated with $(PDAC/TiO_2)_{25}$ along with a pressure gradient to create a high-surface-area photocatalytic region, followed by $(PAMAM/PAA)_{50}$ in the absence of a gradient to create a barrier to CEES transport. On exposure to 3 µl of CEES the mass flux of CEES across the membrane and into the sweep gas is observed in the presence of ultraviolet light as well as in the dark. In both cases a time-lag of 60–90 s is observed, during which the vapour sample is in the capillary of the test system but has not yet reached the detector. Net permeation over the duration of the test is reduced by more than 74% in the presence of ultraviolet light, and peak flux occurs earlier in the test when compared with the dark scenario. This is attributed to ultraviolet absorption, localized heating and material expansion of the thin barrier film restricting CEES permeation.

The spray-LbL platform presents an elegant solution by enabling the application of a mass-transfer-limiting ‘barrier’ layer with controllable properties and thickness directly onto the functionalized membrane using electrostatic assembly of hydrophilic polyelectrolytes. To establish a basis by which

Table 1 | Permeability to CEES and water vapour shown by multifunctionalized samples.

No.		Water-vapour flux ($kg\,m^{-2}$-d^{-1})	Photocatalytic capability	Surface area ($m^2\,g^{-1}$)
1	Saran plastic film + $(PDAC/TiO_2)_{25}$	0.2	0.48	—
2	ES nylon	14.3	0	2.02 ± 0.08
3	ES + vac$(PDAC/TiO_2)_{25}$	14.3	0.15	48.75 ± 1.02
4	ES + vac$(PDAC/TiO_2)_{25}$ over Saran film	0.2	0.87	—
5	ES + vac$(PDAC/TiO_2)_{25}$ + $(PDAC/SPS)_{50}$	12.8	0.58	36.59 ± 0.01
6	ES + vac$(PDAC/TiO_2)_{25}$ + $(PAMAM/PAA)_{50}$	14.2	0.74	19.15 ± 0.30
7	ES + vac$(PDAC/TiO_2)_{25}$ + $(LPEI/PAA)_{100}$	14.2	0.27	—
8	US army cotton battle-dress uniform	12.1	0	—

Measured water-vapour flux and photocatalytic capability of several untreated (nos 2 and 8), photocatalytically functionalized (nos 1, 3 and 4), and multiply functionalized (nos 5–7) samples. Each surface-area range represents values collected from three separate samples deposited from independent solutions. Samples 5 and 6 demonstrate the advantages of conformal TiO_2 treatment as well as pore bridging on available surface area and permeation characteristics. The dramatic increase in surface area observed when as-spun nylon fibres are conformally treated with $(PDAC/TiO_2)_{25}$ coatings does not translate to increased photocatalytic ability until a barrier layer is added to mitigate vapour-phase diffusion through the membrane and increase the residence time for reaction to occur.

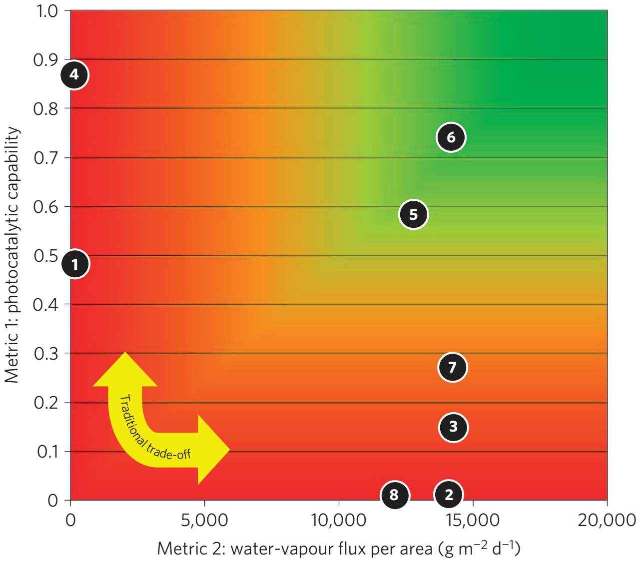

Figure 5 | Observed trade-off between reactive properties and water-vapour transport rates. Graphical representation of data tabulated in Table 1. Traditionally, effective barrier materials (nos 1 and 4) do not possess the high selectivity necessary to discern between water molecules and contaminant molecules, thus sacrificing water-vapour permeability in an effort to limit toxic molecule permeation. Alternatively, highly porous materials (nos 2 and 8) readily permit water-vapour transport, but provide little resistance to hazardous vapours. Multiply functionalized ES materials (nos 5–7) are able to act as tunable asymmetric membranes to optimize the residence time of toxic vapours in the reactive portion of the membrane, improving photocatalytic activity without sacrificing water-vapour permeability.

polyelectrolyte multilayers form an effective barrier layer, the mass-transfer properties of four weak-polyelectrolyte systems were evaluated by spraying non-porous films on microporous polycarbonate substrates. Weak polyelectrolytes vary their degree of ionization as a function of solution pH, presenting a means to manipulate the effective ionic crosslinking of the film as well as the chemical composition independently to tune permeation of CEES molecules through the matrix. Using the time-lag method[30,31] to describe solution-diffusion mass transfer of solute molecules through a non-porous material[32], permeability values were collected for the four polyelectrolyte systems deposited over a range of pH values (see Supplementary Information). Using this technique, the permeability can be broken down into a solubility contribution and a diffusivity contribution. The solubility contribution in LbL films can be interpreted as the relative ease with which solute molecules interact with chemical species present in the polymer film as they traverse the film. The diffusivity contribution reflects the molecular-scale mobility of CEES in the coating. Increased solubility occurs when the energy associated with introducing a solute molecule into the polymer matrix is low, and decreased diffusivity is observed as the charged nature of the polyelectrolyte constituents increases, leading to a more densely crosslinked electrostatic thin film. For example, films deposited from the weak polycation poly(allylamine hydrochloride) (PAH) and the weak polyanion PAA over the pH range 4–8 show very similar CEES permeability values to those observed from films of linear poly(ethyleneimine) (LPEI) and PAA (see Supplementary Information), but for very different reasons. PAH is highly charged below its acid dissociation constant ($pK_a \approx 8.5$), generating more densely crosslinked films, and lower diffusivities, than those created from LPEI ($pK_a \approx 5.5$) for the pH range in question. Similarly, CEES molecules interact more favourably with primary amine groups present in $(PAH/PAA)_n$ films than secondary amines present in $(LPEI/PAA)_n$ films, leading to significantly higher solubility values. The net effect on permeability seems quantitatively similar, but the insight gained by separating the permeability into solubility and diffusivity contributions is invaluable. In an effort to facilitate water-vapour transport while retarding CEES transport, it is necessary to form a mass-transfer-limiting surface layer bridging the network of fibres using polyelectrolyte systems that specifically show low CEES solubility values.

Selecting materials that fit this criterion, we demonstrate the creation of asymmetrically functionalized ES membranes using the weak-polyelectrolyte systems $(LPEI/PAA)_n$ at pH 5 and $(PAMAM/PAA)_n$ at pH 4, as well as the strong polyelectrolyte system $(PDAC/PAA)_n$, as bridging agents (see Supplementary Information for chemical structures). In the absence of convective driving force ($Re_d = 0$), 50 bilayers of the dendritic PAMAM deposition efficiently bridges the surface pores while penetrating less than 30 μm into the 300 μm thick ES membrane. A barrier layer is created near the mat's surface (Fig. 3) reminiscent of asymmetric polymer membranes created by phase inversion[33,34]. In this case, however, the remaining 90% of the mat contains conformal vac$(PDAC/TiO_2)$ functionality, and is capable of degrading contaminant molecules, with the aid of ultraviolet light, during their prolonged residence time in this portion of the membrane. Although it seems fairly porous, the barrier layer visible in the cross-sectional image is capped with a thin, relatively continuous polymer film (Fig. 1d) covering more than 95% of the surface. Furthermore, as the CEES-barrier properties of the $(PAMAM/PAA)_{50}$ region are due primarily to solubility effects, the hydrophilic nature of the sublayer and thin-film skin continues to permit water-vapour permeation. When compared with ES vac(PDAC/TiO_2) material with no bridged layer, ES vac(PDAC/TiO_2) + (PAMAM/PAA)$_{50}$ samples demonstrate an increase in photocatalytic capability from 15 to 74%, while maintaining a water-vapour flux of 14.2 kg m^{-2}-d^{-1} (for comparison, cotton materials typically allow 12–14 kg m^{-2}-d^{-1}, and any material demonstrating flux greater than 1 kg m^{-2}-d^{-1} is categorized as water permeable). This reflects a roughly 0.5% reduction in water-vapour flux compared with non-bridged ES vac(PDAC/TiO_2). Peak flux of CEES under ultraviolet light briefly climbs to similar levels as observed in dark tests (Fig. 4) owing to some vapour diffusion that occurs rapidly through the remaining pores, but sharply recedes as the detoxifying features of the film activate.

For comparison, measured photocatalytic capabilities as well as water-vapour flux rates for ES vac(PDAC/TiO_2) + (PDAC/SPS)$_{50}$ and ES vac(PDAC/TiO_2) + (LPEI/PAA)$_{100}$ are tabulated in Table 1 along with BET surface areas for the two best-performing films. ES vac(PDAC/TiO_2) + (LPEI/PAA)$_{100}$ demonstrated high water-vapour permeability as expected from its low CEES solubility during (LPEI/PAA)$_n$ permeability tests (Note that CEES permeation tests are conducted at ambient humidity, thus solid films that show high water permeability naturally tend to have more moisture present in their matrices. CEES and water mixtures are highly energetically unfavourable, which explains the tendency for high water-vapour solubility, thus permeability, and low CEES solubility to go hand in hand.); however, the low-molecular-weight LPEI (25 k) resulted in a barrier layer with less tendency to bridge the large ES pores. Significant amounts of CEES were therefore able to pass by vapour diffusion, avoiding degradation. Higher-molecular-weight SPS (1 M), in combination with PDAC (150,000), led to a greater degree of pore bridging, as indicated by the membranes' measured surface-area decrease from 48.75 to 36.59 m^2 g^{-1}, thus increasing residence time for photocatalytic activity. Similarly, the effects of less hydrophilic SPS in the barrier region and thin-film skin manifest themselves in reduced water-vapour flux as compared with samples bridged using the high-amine-content PAMAM system. As discussed previously, the traditional trade-off between barrier properties and water-vapour transport is described graphically in Fig. 5. Materials along the axes show either good reactive barrier properties or high water-vapour flux, but not both. The ability to control chemical identity, thickness and degree of bridging in the flux-limiting portion of the membrane enables enhancement of the reactive properties while maintaining membrane breathability, producing an engineered textile that shows the reactive capability of non-porous barrier materials and water-vapour flux similar to that of highly porous untreated ES mats. ES vac(PDAC/TiO_2) + (PAMAM/PAA)$_{50}$ shows a significant decrease in membrane surface area due to the pore-bridging ability of the dendritic PAMAM molecules, as well as high water-vapour flux due to their hydrophilic nature.

Although these results present an attractive improvement on the current chemical protective measures practiced by the US Army, the applications are significantly broader in scope. Demonstrated here for high-efficiency reactive gas purification, the self-cleaning functionalities of these membranes can be extended to water purification, by creating and functionalizing filters with reactive capabilities[35,36], and fabric treatment[21,22,37]. As a readily scalable platform application, this technology also has potential in the large-scale manufacture and treatment of carbon nanotube sheets[38,39], as well as the rapidly developing field of biological and tissue engineering by functionalizing high-surface-area scaffolds with proteins[40–44]. As the challenges of generating more complex polymer-based membrane systems require engineers to impart new functionalities to materials without sacrificing mechanical robustness[45] or ease of manufacturing, LbL spray-coating of porous non-wovens provides the versatility to control nanoscale features and functionality on the macroscopic level. Specialized technologies can now be developed in industrially significant quantities using a rapid, yet inexpensive, scalable approach.

Methods

ES materials synthesis. Non-woven meshes of nylon fibres were made by electrospinning a solution of 10% nylon 6,6 (45,000 M_w) (Scientific Polymer Products) in hexafluoroisopropanol (Aldrich) at 0.1 ml min^{-1} with a needle-to-collector distance of 31 cm and a source voltage of 26.8 kV for 40 min using a parallel-plate electrospinning apparatus[17]. Mats were soaked in a 0.02 M aqueous solution of PAH (56,000 M_w) (Aldrich) for 30 min before LbL treatment.

LbL film assembly. LPEI (25,000 M_w) (Polysciences), PAA (15,000 M_w, 35% aqueous solution) (Aldrich), PAMAM (G4, 22% solution in methanol) (Dendritech), SPS (1,000,000 M_w) (Aldrich) and PDAC (150,000 M_w, 20% aqueous solution) (Aldrich) were used as received and prepared as 0.02 M solutions, on the basis of the repeat-unit molecular weight, in Milli-Q water. A colloidal solution of TiO_2 nanoparticles was synthesized as reported previously[29], and diluted to a concentration of 1.65 mg ml^{-1}. Mats were first treated using a vacuum-assisted spray-LbL technique by alternately spraying with PDAC and TiO_2 solutions titrated to pH 10 to develop 25-bilayer coatings. Mats were then flipped and sprayed with either PAMAM and PAA titrated to pH 4 or SPS and PDAC titrated to pH 10 to develop 50-bilayer coatings, or LPEI and PAA titrated to pH 5 to develop 100-bilayer coatings. For further details of the spray-LbL process please see Supplementary Information.

Characterization. Mats were coated with a 10 nm layer of Au/Pd and imaged using a JEOL JSM-6060 scanning electron microscope. Average fibre diameter was determined by measuring 40–60 individual fibres on both sides of the ES mat. Surface-area measurements were performed by BET (Micromeritics, ASAP 2020), and verified using both nitrogen and krypton as the adsorbent gas.

Permeation testing. Treated mats were mounted in a stainless-steel permeation cell and subjected to a saturated vapour of CEES (Aldrich) evolving from a 3 µl drop[29]. Meanwhile, a stream of ultrapure compressed air (AirGas) was passed at 50 SCCM beneath the sample and analysed using a Total Hydrocarbon Analyser (Gow-MAC Instruments, Series 23-550) equipped with a flame ionization detector. During ultraviolet testing the photocatalytic side of the material was also exposed to a ultraviolet spot source (Dymax, Blue Wave 200) filtered to 50 mW cm^{-2} intensity. Note that, although CEES is a less toxic simulant for HD mustard gas, extreme caution should still be exercised when working with it. Water-vapour permeation tests were conducted using a Dynamic Moisture Permeation Cell[46] by passing air at two different relative humidities over opposite sides of the treated mat, and measuring the change in water vapour in each stream.

Received 1 December 2008; accepted 19 March 2009;

References

1. Bretsche, M. S. Membrane structure—some general principles. *Science* **181**, 622–629 (1973).
2. Rothman, J. E. & Lenard, J. Membrane asymmetry. *Science* **195**, 743–753 (1977).
3. Sridhar, S., Smitha, B. & Aminabhavi, T. M. Separation of carbon dioxide from natural gas mixtures through polymeric membranes—a review. *Sep. Purif. Rev.* **36**, 113–174 (2007).
4. Decher, G. Fuzzy nanoassemblies: Toward layered polymeric multicomposites. *Science* **277**, 1232–1237 (1997).
5. Shiratori, S. S. & Rubner, M. F. pH-dependent thickness behavior of sequentially adsorbed layers of weak polyelectrolytes. *Macromolecules* **33**, 4213–4219 (2000).
6. Dubas, S. T. & Schlenoff, J. B. Factors controlling the growth of polyelectrolyte multilayers. *Macromolecules* **32**, 8153–8160 (1999).
7. Lee, D., Rubner, M. F. & Cohen, R. E. All-nanoparticle thin-film coatings. *Nano Lett.* **6**, 2305–2312 (2006).
8. Lvov, Y., Ariga, K., Onda, M., Ichinose, I. & Kunitake, T. Alternate assembly of ordered multilayers of SiO_2 and other nanoparticles and polyions. *Langmuir* **13**, 6195–6203 (1997).
9. Iler, R. K. Multilayers of colloidal particles. *J. Colloid Interface Sci.* **21**, 569–594 (1966).
10. Caruso, F., Caruso, R. A. & Mohwald, H. Nanoengineering of inorganic and hybrid hollow spheres by colloidal templating. *Science* **282**, 1111–1114 (1998).
11. Yoo, P. J. *et al.* Spontaneous assembly of viruses on multilayered polymer surfaces. *Nature Mater.* **5**, 234–240 (2006).
12. Tang, Z. Y., Wang, Y., Podsiadlo, P. & Kotov, N. A. Biomedical applications of layer-by-layer assembly: From biomimetics to tissue engineering. *Adv. Mater.* **18**, 3203–3224 (2006).
13. Hammond, P. T. Form and function in multilayer assembly: New applications at the nanoscale. *Adv. Mater.* **16**, 1271–1293 (2004).

14. Schlenoff, J. B., Dubas, S. T. & Farhat, T. Sprayed polyelectrolyte multilayers. *Langmuir* **16**, 9968–9969 (2000).
15. Izquierdo, A., Ono, S. S., Voegel, J. C., Schaaff, P. & Decher, G. Dipping versus spraying: Exploring the deposition conditions for speeding up layer-by-layer assembly. *Langmuir* **21**, 7558–7567 (2005).
16. Krogman, K. C., Zacharia, N. S., Schroeder, S. & Hammond, P. T. Automated process for improved uniformity and versatility of layer-by-layer deposition. *Langmuir* **23**, 3137–3141 (2007).
17. Fridrikh, S. V., Yu, J. H., Brenner, M. P. & Rutledge, G. C. Controlling the fiber diameter during electrospinning. *Phys. Rev. Lett.* **90**, 144502 (2003).
18. Chen, L., Bromberg, L., Hatton, T. A. & Rutledge, G. C. Electrospun cellulose acetate fibers containing chlorhexidine as a bactericide. *Polymer* **49**, 1266–1275 (2008).
19. Lee, J. A. *et al.* Highly reactive multilayer-assembled TiO_2 coating on electrospun polymer nanofibers. *Adv. Mater.* **21**, 1252–1256 (2009).
20. Chen, L. *et al.* Chemical protection fabrics via surface oximation of electrospun polyacrylonitrile fiber mats. *J. Mater. Chem.* (2009, in the press).
21. Blossey, R. Self-cleaning surfaces—virtual realities. *Nature Mater.* **2**, 301–306 (2003).
22. Daoud, W. A. *et al.* Self-cleaning keratins. *Chem. Mater.* **20**, 1242–1244 (2008).
23. Peercy, P. S. The drive to miniaturization. *Nature* **406**, 1023–1026 (2000).
24. Simon, P. & Gogotsi, Y. Materials for electrochemical capacitors. *Nature Mater.* **7**, 845–854 (2008).
25. Tarascon, J. M. & Armand, M. Issues and challenges facing rechargeable lithium batteries. *Nature* **414**, 359–367 (2001).
26. Yoon, J. *et al.* Ultrathin silicon solar microcells for semitransparent, mechanically flexible and microconcentrator module designs. *Nature Mater.* **7**, 907–915 (2008).
27. Shin, Y. M., Hohman, M. M., Brenner, M. P. & Rutledge, G. C. Experimental characterization of electrospinning: The electrically forced jet and instabilities. *Polymer* **42**, 9955–9967 (2001).
28. Deen, W. M. *Analysis of Transport Phenomena* 6th edn (Oxford Univ. Press, 1998).
29. Krogman, K. C., Zacharia, N. S., Grillo, D. M. & Hammond, P. T. Photocatalytic layer-by-layer coatings for degradation of acutely toxic agents. *Chem. Mater.* **20**, 1924–1930 (2008).
30. Crank, J. *The Mathematics of Diffusion* 2nd edn (Oxford Univ. Press, 1975).
31. Frisch, H. L. Time lag in transport theory. *J. Chem. Phys.* **36**, 510–516 (1962).
32. Wijmans, J. G. & Baker, R. W. The solution-diffusion model: A review. *J. Membrane Sci.* **107**, 1–21 (1995).
33. Peinemann, K., Abetz, V. & Simon, P. F. W. Asymmetric superstructure formed in a block copolymer via phase separation. *Nature Mater.* **6**, 992–996 (2007).
34. Mi, F. *et al.* Fabrication and characterization of a sponge-like asymmetric chitosan membrane as a wound dressing. *Biomaterials* **22**, 165–173 (2001).
35. Shannon, M. A. *et al.* Science and technology for water purification in the coming decades. *Nature* **452**, 301–310 (2008).
36. Corry, B. Designing carbon nanotube membranes for efficient water desalination. *J. Phys. Chem. B* **112**, 1427–1434 (2008).
37. Ma, M. L. *et al.* Decorated electrospun fibers exhibiting superhydrophobicity. *Adv. Mater.* **19**, 255–259 (2007).
38. Cao, Q. *et al.* Medium-scale carbon nanotube thin-film integrated circuits on flexible plastic substrates. *Nature* **454**, 495–500 (2008).
39. Hall, L. J. *et al.* Sign change of Poisson's ratio for carbon nanotube sheets. *Science* **320**, 504–507 (2008).
40. Barnes, C. P., Sell, S. A., Boland, E. D., Simpson, D. G. & Bowlin, G. L. Nanofiber technology: Designing the next generation of tissue engineering scaffolds. *Adv. Drug Delivery Rev.* **59**, 1413–1433 (2007).
41. Dankers, P. Y. W., Harmsen, M. C., Brouwer, L. A., Van Luyn, M. J. A. & Meijer, E. W. A modular and supramolecular approach to bioactive scaffolds for tissue engineering. *Nature Mater.* **4**, 568–574 (2005).
42. Grafahrend, D. *et al.* Control of protein adsorption on functionalized electrospun fibers. *Biotechnol. Bioeng.* **101**, 609–621 (2008).
43. Heydarkhan-Hagvall, S., Schenke-Layland, K. & Dhanasopon, A. P. Three-dimensional electrospun ECM-based hybrid scaffolds for cardiovascular tissue engineering. *Biomaterials* **29**, 2907–2914 (2008).
44. Zhang, X. H., Baughman, C. B. & Kaplan, D. L. In vitro evaluation of electrospun silk fibroin scaffolds for vascular cell growth. *Biomaterials* **29**, 2217–2227 (2008).
45. Park, J. H., Kim, B. S., Yoo, Y. C., Khil, M. S. & Kim, H. Y. Enhanced mechanical properties of multilayer nano-coated electrospun nylon 6 fibers via a layer-by-layer self-assembly. *J. Appl. Polym. Sci.* **107**, 2211–2216 (2008).
46. Gibson, P. W., Kendrick, C. E. & Rivin, D. Apparatus and method for determining transport properties of porous materials. US Patent No. 6,119,506 (1999).

Acknowledgements

This research was supported in part by the US Army through the Institute for Soldier Nanotechnologies under contract DAAD-19-02-0002 with the US Army Research Office, and by the G. Nicholas and Dorothea K. Dumbros Scholarship and Fellowship Fund. The content does not necessarily reflect the position of the government, and no official endorsement should be inferred. The authors would like to thank H. Schreuder-Gibson and P. Gibson of the US Army Soldier Systems Center for assistance with water-vapour permeation testing.

Additional information

Supplementary information accompanies this paper on www.nature.com/naturematerials. Reprints and permissions information is available online at http://npg.nature.com/reprintsandpermissions. Correspondence and requests for materials should be addressed to P.T.H.